

Performance of Philips Gemini TF PET/CT Scanner with Special Consideration for Its Time-of-Flight Imaging Capabilities

Suleman Surti¹, Austin Kuhn¹, Matthew E. Werner¹, Amy E. Perkins², Jeffrey Kolthammer³, and Joel S. Karp¹

¹Department of Radiology, University of Pennsylvania, Philadelphia, Pennsylvania; ²Philips Research, Briarcliff, New York; and

³Philips Medical Systems, Highland Heights, Ohio

Results from a new PET/CT scanner using lutetium-yttrium oxyorthosilicate (LYSO) crystals for the PET component are presented. This scanner, which operates in a fully 3-dimensional mode, has a diameter of 90 cm and an axial field of view of 18 cm. It uses $4 \times 4 \times 22$ mm³ LYSO crystals arranged in a pixelated Anger-logic detector design. This scanner was designed to perform as a high-performance conventional PET scanner as well as provide good timing resolution to operate as a time-of-flight (TOF) PET scanner. **Methods:** Performance measurements on the scanner were made using the National Electrical Manufacturers Association (NEMA) NU2-2001 procedures to benchmark its conventional imaging capabilities. The scatter fraction and noise equivalent count (NEC) measurements with the NEMA cylinder (20-cm diameter) were repeated for 2 larger cylinders (27-cm and 35-cm diameter), which better represent average and heavy patients. New measurements were designed to characterize its intrinsic timing resolution capability, which defines its TOF performance. Additional measurements to study the impact of pulse pileup at high counting rates on timing, as well as energy and spatial, resolution were also performed. Finally, to characterize the effect of TOF reconstruction on lesion contrast and noise, the standard NEMA/International Electrotechnical Commission torso phantom as well as a large 35-cm-diameter phantom with both hot and cold spheres were imaged for varying scan times. **Results:** The transverse and axial resolution near the center is 4.8 mm. The absolute sensitivity of this scanner measured with a 70-cm-long line source is 6.6 cps/kBq, whereas scatter fraction is 27% measured with a 70-cm-long line source in a 20-cm-diameter cylinder. For the same line source cylinder, the peak NEC rate is measured to be 125 kcps at an activity concentration of 17.4 kBq/mL (0.47 μ Ci/mL). The 2 larger cylinders showed a decrease in the peak NEC due to increased attenuation, scatter, and random coincidences, and the peak occurs at lower activity concentrations. The system coincidence timing resolution was measured to be 585 ps. The timing resolution changes as a function of the singles rate due to pulse pileup and could impact TOF image reconstruction. Image-quality measurements with the torso phantom show that very high quality images can be obtained with short scan times (1–2 min per bed position). However, the benefit of TOF is more apparent with

the large 35-cm-diameter phantom, where small spheres are detectable only with TOF information for short scan times. **Conclusion:** The Gemini TF whole-body scanner represents the first commercially available fully 3-dimensional PET scanner that achieves TOF capability as well as conventional imaging capabilities. The timing resolution is also stable over a long duration, indicating the practicality of this device. Excellent image quality is achieved for whole-body studies in 10–30 min, depending on patient size. The most significant improvement with TOF is seen for the heaviest patients.

Key Words: PET; PET/CT; time-of-flight PET; fully 3-dimensional whole-body imaging; lutetium-yttrium oxyorthosilicate

J Nucl Med 2007; 48:471–480

The Gemini TF PET/CT (Philips Medical Systems) is a new high-performance, time-of-flight (TOF) capable, fully 3-dimensional (3D) PET scanner together with a 16-slice Brilliance CT scanner. It was installed at the University of Pennsylvania PET Center in November 2005 and, after a period of evaluation and performance of research studies, is now being routinely used for clinical studies since May 2006. The PET scanner uses small, discrete lutetium-yttrium oxyorthosilicate ([LYSO], with the Lu-to-Yt ratio of 9:1) crystals placed in an Anger-logic detector design to achieve uniform light spread in the detector. The fast timing properties, high light output, and high stopping power of LYSO combined with this detector design lead to a high-sensitivity scanner with good counting rate capability and very good spatial, energy, and timing resolutions. The timing resolution of this PET scanner enables a precise TOF measurement for the coincident photons from each annihilation event. In this study, we evaluated the imaging characteristics of the PET component of the Gemini TF scanner using the National Electrical Manufacturers Association (NEMA) NU2-2001 standards measurements (*I*), as well as additional measurements to evaluate its intrinsic TOF capability and its impact on the reconstructed images.

Received Jul. 28, 2006; revision accepted Nov. 21, 2006.

For correspondence or reprints contact: Suleman Surti, PhD, Department of Radiology-HUP, 3400 Spruce St., Philadelphia, PA 19104.
E-mail: surti@mail.med.upenn.edu

MATERIALS AND METHODS

PET Scanner Design and Intrinsic Measurements

Detector and Electronics. The PET component of the Gemini TF is composed of 28 flat modules of a 23×44 array of $4 \times 4 \times 22$ mm³ LYSO crystals. The individual modules are coupled together in the transverse direction leading to a scanner ring diameter of 90.34 cm. A 2.5-cm-thick annulus of lead shielding at the 2 axial ends is used to reduce detection of events from outside the field of view (FOV). The patient bore has a diameter of 71.7 cm with active transverse and axial FOVs of 57.6 and 18 cm, respectively. Signal readout is performed by a hexagonal array of four-hundred twenty 39-mm-diameter photomultiplier tubes (PMTs). This detector design was derived from the pixelated gadolinium oxy-orthosilicate Anger-logic detector (2) used in the G-PET brain scanner (3) and followed by the commercial whole-body Allegro (4) and Gemini (5,6) scanners from Philips (PIXELAR technology). The Anger-logic detector has characteristics of good crystal separation with uniform light collection and energy resolution. Electronic signal digitization is performed by 100-MHz flash (asynchronous) analog-to-digital converters for each PMT with 9 samples added, corresponding to an equivalent integration time of 90 ns. Concurrently, the PMT signals are also summed into 28 trigger channels, each consisting of a group of 20 PMTs. Each trigger signal passes through a leading-edge discriminator to obtain timing information for high-energy deposition events in the detector. The hardware coincidence-timing window for this scanner is set at 6 ns, and a delayed coincidence window technique is used to estimate the random coincidences in collected data.

Energy and Timing Calibrations. To obtain good energy resolution uniformly over the detector, there are 2 primary sources of error that need to be corrected with energy calibration techniques: variations in individual PMT gains as well as variations in collected light from individual crystals, which depends on the crystal itself but, primarily, on its position relative to the PMT array within the detector. Correction tables are generated by using a ²²Na point source and calculating the peak position in the energy spectrum for each crystal and normalizing it to a common value. The system energy resolution averaged over all crystals after correction is 11.5% full width at half maximum (FWHM) at 511 keV, which allows the default energy window to be set at 440–665 keV.

Because this scanner was designed to provide accurate timing information for each annihilation event, the system timing calibrations need to be performed accurately and in an easily reproducible manner. The timing calibrations are once again a function of the individual PMT timing offset as well as the crystal and its position in the detector relative to the PMT array. For timing calibrations, a ²²Na point source in a brass block is placed at the center of the scanner. The difference in arrival times for all unscattered and scattered coincident photons is recorded and timing histograms are generated for all possible lines of response (LORs). The source position and, hence, the correct difference in arrival times are also known (zero for a centered source). A timing correction factor is then generated for each LOR as the difference in the centroid of its measured timing histogram versus the correct difference in arrival time (7). The system timing resolution for this scanner averaged over all crystals after timing offset corrections is 585 ps (FWHM) for a point source in air. In Figure 1, we plot the measured timing resolution from the daily quality control test over a period of 6 mo (from December 2005 to May 2006). The timing resolution measured with the calibration source was initially 630 ps,

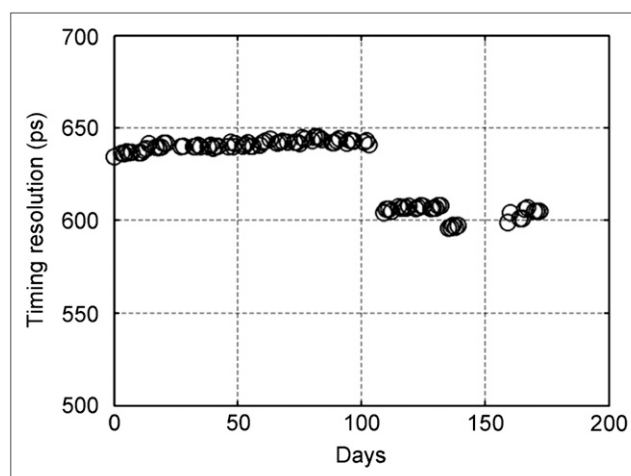


FIGURE 1. Plot of daily timing resolution as measured with rod source over a period of several months. Improvements represent software calibration upgrades that took place over this time period.

which—after hardware and calibration upgrades in March 2006 (110 d in Fig. 1)—improved to the current value of about 600 ps. Note that the calibration source is a point source placed in a brass block, which degrades the timing resolution slightly due to scatter when compared with the result from a point source in air. The constant value of the measured system timing resolution demonstrates the stability of the electronics developed for this system.

Impact of Counting Rate on Timing, Energy, and Spatial Resolution. Pulse pileup at high counting rates, which affects energy and spatial resolution in conventional PET scanners (8) to varying degrees, can also impact the timing resolution of the TOF PET scanners. Because the timing resolution is used in the TOF reconstruction algorithm, it is important to characterize the timing resolution of TOF PET scanners for varying counting rates. For this purpose we used a small (<0.3 mm) ²²Na point source (half-life, 2.6 y) placed at the center of the scanner (Fig. 2A). Placed axially on either side of this point source are two 20-cm-diameter \times 30-cm-long water-filled cylinders with a high amount (700 MBq [19 mCi]) of ¹⁸F activity (half-life, 109 min). These cylinders were placed 5 cm apart axially from each other with the point source centered in between. Data were collected in list mode for all coincident events along with their time stamps over multiple time points as the ¹⁸F decayed over several half-lives. For each time point (or activity level), the data were filtered so that analysis was performed only on those LORs that lay within the central 4 cm axially (centered over the point source) and the central 3 cm in radial bins (centered over the point source). Almost all of these LORs originate from positron annihilations in the ²²Na point source and represent the true coincidences. After restricting the LORs to those from the point source, histograms were generated for the difference in arrival times of the 2 coincident photons from the list data. Additionally, the data were also binned in separate histograms to measure energy and spatial resolution (in sinogram space) as functions of the counting rate.

Scanner Performance Measurements

Performance measurements were done on the Gemini TF scanner following the procedure outlined in the NEMA NU2-

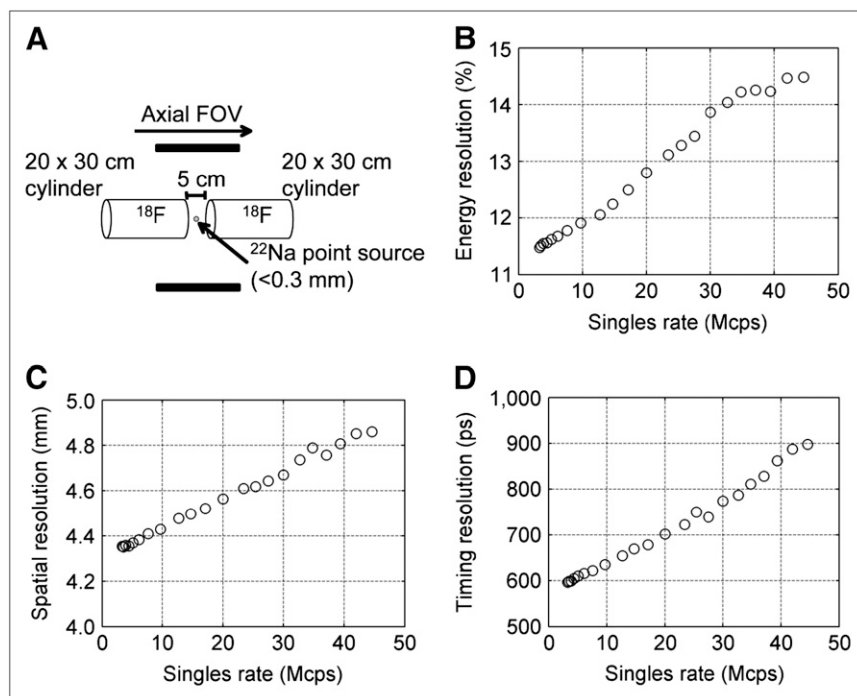


FIGURE 2. (A) Experimental setup for measuring energy, spatial, and timing resolution with a point source as a function of counting rate in scanner. (B) Measured energy, (C) detector spatial (sinogram space), and (D) timing resolutions are shown as functions of singles rate in scanner. Currently, clinical imaging is performed at a singles rate of 15–25 Mcps.

2001 standard (1). Additional measurements were also performed to fully evaluate the characteristics of this scanner, including its TOF imaging capability.

Spatial Resolution. Spatial resolution measurements were performed using a point source of ^{18}F in a thin glass capillary tube with an inner diameter of <1 mm. The axial length of the point source was also kept at <1 mm. Following the NU2-2001 protocol, measurements were performed at radial positions of 1 and 10 cm. The sinograms for prompt and delayed count data were binned in 15 tilt angles with 2-mm sampling in the transverse and axial directions. The delayed sinogram at each source position was subtracted from the prompts sinograms to account for the coincidence counts arising from the intrinsic radioactivity of ^{176}Lu (9,10). The subtracted sinograms were then reconstructed using the 3D Fourier reprojection (3D-FRP) algorithm (11), with an unapodized filter (ramp filter with a cutoff at the Nyquist frequency). The NEMA measurement specifies that the image pixel size should be smaller than one third of the expected FWHM. The images were reconstructed into a $576 \times 576 \times 180$ array. Standard NEMA analysis was then performed to calculate the FWHM and the full width at tenth maximum (FWTM) of the point spread functions in all 3 directions.

Sensitivity. Following the NEMA NU2-2001 standard, the absolute sensitivity of the Gemini TF scanner was measured using a 70-cm-long line source at the center of the scanner, without and with 4 different metal sleeves representing varying amounts of attenuation. This measurement technique is based on work described previously by Bailey et al. (12). The sensitivity measurement was performed using the standard energy window of 440–665 keV.

Scatter. The scatter fraction (SF) for the Gemini TF scanner was measured following the NU2-2001 procedure with some modifications to account for the counts arising due to the intrinsic radioactivity of ^{176}Lu (9,10). The measurement uses a line source filled with ^{18}F , placed at a 4.5-mm radial offset from the center of

a solid polyethylene cylinder (diameter, 20 cm; length, 70 cm) with a water equivalent density of 1 g/mL. The tube is 70-cm long with a volume of about 5.7 mL. This phantom is equivalent in attenuation and scatter properties to a uniform, water-filled cylinder of similar size. The prompt and delayed coincidence window data were acquired at low counting rates and rebinned using single-slice rebinning (13). The delayed sinogram profile was used to calculate the number of random events within an object diameter of 24 cm (4 cm larger than the phantom diameter) for each slice i (R_i). Similarly, the prompt sinogram profile was used to calculate the number of nontrue (scatter and random) events within an object diameter of 24 cm, as well as the number of true coincidences within a 2-cm radius of the source. The nontrue counts within the peak were estimated by assuming a constant background under the peak, the level of which was determined by the average of the intensities near the edge of the peak (at ± 2 cm). The random counts as estimated by R_i from the delayed sinogram were then subtracted from the nontrue counts in the prompt sinogram on a slice-by-slice basis to calculate the scatter counts in i th slice (S_i). System SF is then defined as:

$$SF = \frac{\sum_i S_i}{\sum_i (S_i + T_i)} \quad \text{Eq. 1}$$

These measurements were performed as a function of lower-level discriminator (ELLD for energy lower-level discriminator) while keeping the upper gate fixed at 665 keV. The data acquisition was performed in list mode, and sinogram rebinning was subsequently performed on the data using different ELLD values. To better assess the performance of the scanner for heavy patients, we manufactured 2 annular polyethylene sleeves of inner diameters 20 and 27 cm and outer diameters of 27 and 35 cm, respectively. Using the sleeve with the 27-cm outer diameter, we achieve an effective cylinder diameter of 27 cm (representative of

an average patient). Similarly, using the 35-cm outer diameter sleeve over this setup results in a cylinder with an effective diameter of 35 cm (representative of a heavy patient) (14). The calculation of scatter was performed within regions of 31 and 39 cm (diameter of cylinder + 4 cm)—analogous to the NEMA prescription for the 20-cm-diameter phantom.

Counting Rate Performance. For counting rate performance in a whole-body imaging situation, the NEMA NU2-2001 standard using the 20-cm-diameter \times 70-cm-long line source cylinder as well as the 27-cm-diameter \times 70-cm-long cylinder and the 35-cm-diameter \times 70-cm-long cylinder were used. The line source in these measurements was filled with an aqueous solution of ^{18}F with an initial activity level ranging from 520 to 660 MBq (14–18 mCi). These measurements were performed with the default energy window at 440–665 keV. Data were acquired at several time points as activity decayed in the cylinders. True, scattered, and random coincidences were calculated in the same way as described for the *SF* measurement using the separately binned prompts and delays sinograms. Noise equivalent counts, or *NEC*, were calculated using the relation:

$$NEC = \frac{T \times T}{T + Sc + kR}, \quad \text{Eq. 2}$$

where *T* is the true, *Sc* is scatter, *R* is random counting rate within the object diameter, and *k* is set to 1 or 2 depending on whether we use direct randoms subtraction or use variance reduction techniques for estimating a smooth randoms distribution. Recent effort at extending this *NEC* formula for TOF scanners (15) indicates that the random counting rate over the object diameter (*R*) as shown in Equation 2 is reduced by a factor equal to the scanner FOV divided by the object diameter. However, this reduction in randoms, and a consequent increase in the *NEC* of TOF scanners, is not used in our calculations here.

Image Quality. Image-quality measurements were performed using 6 spheres in the NEMA/International Electrotechnical Commission (IEC) torso phantom that also contains a cylindric foam insert with a diameter of 50 mm and a density of 0.3 g/cm³. The spheres had internal diameters (*d_i*) of 37, 28, 22, 17, 13, and 10 mm and were placed so that their centers lay in the same axial plane close to the central slice in the scanner. The 2 largest spheres were cold, whereas the 4 smaller spheres were filled with an activity concentration of 4:1 with respect to the background. To simulate activity outside the FOV, the 20 \times 70 cm line source cylinder was placed adjacent to the torso phantom and outside the scan FOV. Standard NEMA analysis was performed by drawing circular regions of interest (ROIs) on the spheres as well as 60 background regions. In this manner, the contrast recovery coefficient (*CRC*) and background variability as defined by NEMA were calculated for each sphere. In addition, relative noise in each background region was estimated as the ratio of the SD of counts to the mean counts in that region. An average of this relative noise for all 60 background ROIs was then used as the value of pixel noise for a given sphere size.

The starting activity concentration of ^{18}F in the phantom background was about 8.5 kBq/mL (0.23 $\mu\text{Ci/mL}$). Data were acquired so that 3 independent replicates corresponding to imaging times of 1 min and 3 min were reconstructed. For TOF reconstruction, we used the list-mode reconstruction (distributed list-mode TOF, DLT) implemented by Philips that is based on a TOF list-mode maximum-likelihood algorithm that was originally

developed in our laboratory at the University of Pennsylvania (16,17). This algorithm models data corrections in the algorithm and uses consecutively ordered subsets. We reconstruct these phantom studies using the clinical patient protocol defined at the University of Pennsylvania that uses unrelaxed ordered-subsets expectation maximization (OSEM) ($\lambda = 1$) with 33 subsets and stops after 3 iterations for practical reconstruction time. Note that the scan and reconstruction times at the University of Pennsylvania are longer than those defined as default by Philips and represent our desire to better understand the imaging capabilities of this scanner. Because this scanner operates in a TOF mode and the full benefits of TOF information on clinical diagnosis are still being investigated, we elected to be conservative in choosing longer scan times (and, hence, reconstruction times as well due to list-mode reconstruction) for our patient imaging. With a scan time of 3 min per bed position, a fully corrected image is completed 25–50 min after the end of the scan for a 9-bed-position study (axial extent of 90 cm). Preprocessing of attenuation factors and scatter begins after collection of the first bed position. The image reconstruction is performed in parallel over ten 3.6-GHz Intel Xeon dual-processor machines and results in an image reconstruction time of 3.8 s for 1 million prompt coincidences. Attenuation correction was performed using the CT transmission data, whereas scatter is currently estimated using a non-TOF model-based single-scatter simulation (SSS) (18). In addition, we sorted the data into sinograms and reconstructed using a fully 3D, LOR-based iterative reconstruction algorithm (row-action maximum-likelihood algorithm, or LOR RAMLA) (19–21).

To study the behavior of *CRC* and noise with a number of iterations, we implemented a TOF extended SSS algorithm for scatter estimation in both time and radial bins, in the University of Pennsylvania (UPenn) list-mode reconstruction algorithm. The TOF extended SSS algorithm is similar conceptually to that recently presented by Watson (22). For this study we set $\lambda = 1$ but varied the number of iterations from 1 to 10 using 20 subsets.

To better characterize the TOF imaging capability of the Gemini TF with heavy patients, we performed additional measurements using the 6 spheres in a larger 35-cm-diameter phantom (about 55-cm long). The total volume of this phantom is 52,600 mL. To simulate activity outside the FOV, a 20-cm-diameter \times 30-cm-long cylinder was placed axially adjacent to this cylinder. Data were acquired at a total activity of 259 MBq (7.0 mCi) in the 2 phantoms, corresponding to an activity concentration of 4.1 kBq/mL (0.11 $\mu\text{Ci/mL}$) at the beginning of the scan. Data reconstruction was once again performed with the UPenn list-mode reconstruction algorithm for varying acquisition times with 3 replicates for each.

Patient Studies. To correlate cylindric phantom counting rate data to patient studies, we used reconstructed images from several patient studies to measure the girth or diameter of a patient. In our current protocol, we inject patients with 555 MBq (15 mCi) of ^{18}F -FDG and start scanning 60 min after injection. These data represent the general spread of patient population size we typically see in our clinic. In addition, we also calculated a modified *NEC* rate (*NEC'*) as defined by:

$$NEC' = \frac{(T + Sc) \times (T + Sc)}{T + Sc + R} = \frac{(P - D)^2}{P}, \quad \text{Eq. 3}$$

where *P* is the rate of prompt coincidences and *D* is the rate of coincidences collected in the delayed window. This definition,

instead of the standard *NEC* definition (Eq. 2), was used here because of the ease in dealing with clinical data where the *SF* value is not available. For our results, the knowledge of *SF* will add a scale factor to the *NEC'* value that will be a function of patient size and shape. When comparing patients with similar sizes, the relative differences between *NEC'* will be the same as those in the *NEC*.

For illustration, we have included images for a whole-body scan of a patient weighing 61 kg (body mass index [BMI] of 22.2). This patient was injected with 518 MBq (14.0 mCi) of ^{18}F -FDG 60 min before scan time, and data were acquired for up to 3 min per bed position for a total of 8 bed positions. In addition, we also show whole-body images of a heavy patient (115 kg and BMI of 38.0) who was injected with 537 MBq (14.5 mCi) of ^{18}F -FDG 60 min before scan time. Data were again acquired for up to 3 min per bed position for a total of 9 bed positions.

RESULTS

Intrinsic Measurements of Count-Rate Behavior

Figure 2 illustrates the changes in energy resolution (Fig. 2B), spatial resolution (Fig. 2C), and timing resolution (Fig. 2D), which are plotted as a function of the singles rate in the scanner. These results show that there is a small degradation in energy and spatial resolution due to pulse pileup and a change in timing resolution that needs to be properly accounted for in image reconstruction. The effect of the small degradation in the energy resolution affects the calculated *SF* as the default energy window (440–665 keV) is fixed.

Scanner Performance Measurements

Spatial Resolution. Table 1 summarizes the spatial resolution measurement results for the Gemini TF scanner. The spatial resolution near the center is about 4.8 mm in both the transverse and the axial directions (wide profile, NEMA NU2-2001). Moving the point source to a 10-cm radial position results in a small degradation in the transverse resolution of 5.2 mm due to parallax error, whereas the axial resolution remains unchanged at 4.8 mm.

Sensitivity. The absolute sensitivity of the Gemini TF scanner with standard energy window is 6.6 cps/kBq when the line source is placed at the center of the scanner. The axial sensitivity profile is triangular in shape (Fig. 3A) and peaks at about 0.15 cps/kBq.

Scatter. Figure 3B shows the measured *SF* as a function of ELLD for the 20×70 -cm, 27×70 -cm, and 35×70 -cm line source phantoms. These results indicate that by raising the ELLD the *SF* is reduced as expected. The *SF* increases

for all ELLD value as the phantom size increases due to increased attenuation and scatter. At the default ELLD value of 440 keV, the *SF* is measured to be 27%, 35%, and 45% for the 20-, 27-, and 35-cm-diameter cylinders, respectively.

Counting Rate Performance. Figure 4A summarizes the results from counting rate measurements for the 3 cylindrical phantoms. We see reduced true coincidences due to increased attenuation in the larger cylinders leading to reduced *NEC* values as well. In Figures 4B we plot the *NEC* curves for the 3 cylinders as a function of activity concentration as well as the singles rate in the scanner. The peak *NEC* rate is 125, 62, and 24 kcps for the 20-, 27-, and 35-cm-diameter cylinders, respectively, and occurs at activity concentrations of 17.4 kBq/mL (0.47 $\mu\text{Ci/mL}$), 11.8 kBq/mL (0.32 $\mu\text{Ci/mL}$), and 7.8 kBq/mL (0.21 $\mu\text{Ci/mL}$). As a function of singles rate, the peak *NEC* rate is achieved within a singles counting rate range of 25–35 Mcps. In Figure 3C we plot the *SF* as a function of the singles rate for the counting rate performance measurements. As seen in this plot, there is a small increase in the collected scatter coincidences as a function of the singles rate. This increase, however, is properly included in the calculation of the *NEC* rates indicated earlier.

Image Quality. Central slices from images for the NEMA torso phantom with scan times of 1 and 3 min are shown in Figure 5A for TOF and non-TOF reconstructions. These images are after 10 iterations and have similar noise characteristics for the TOF and non-TOF reconstructions. However, the contrast for the small spheres (especially the 10-mm-diameter sphere) is slightly higher with the TOF reconstruction. Note that the error in this comparison is reduced with identical datasets. In Figure 5B we show the central slice for 3- and 5-min acquisitions with the 35-cm-diameter phantom for TOF and non-TOF reconstructions. Once again, the noise characteristics for TOF and non-TOF images are similar for the same iteration number (10, as shown here). However, the increased contrast for the small spheres with TOF information is now clearly demonstrated. In fact, the 10-mm-diameter sphere is not visible in the non-TOF reconstruction even after a 5-min scan, whereas it is easily detectable after 3 min and TOF reconstruction. In Table 2 we show the *CRC* and *Variability* for the torso phantom as measured after TOF and non-TOF reconstructions (after 6 iterations) with our research reconstruction algorithm for a 3-min scan time. In addition, we also show the numbers for the non-TOF LOR RAMLA and TOF DLT reconstructions.

Quantitatively, we plot *CRC* against *Noise* for the torso phantom and the 35-cm-diameter phantom in Figure 6. We show results for the 13-mm-diameter hot sphere after a 3-min scan time. We clearly see that there is no significant improvement in image quality (in terms of *CRC* and *Noise*) with TOF information in the torso phantom. However, the *CRC* value converges at a faster rate to its highest value (fewer iterations), leading to somewhat reduced noise in the

TABLE 1
Results from Spatial Resolution Measurements with a Point Source

Parameter	Radial position: $r = 1$ cm		Radial position: $r = 10$ cm		
	Transverse	Axial	Radial	Tangential	Axial
FWHM (mm)	4.8	4.8	5.2	5.2	4.8
FWTM (mm)	9.7	9.6	10.3	10.2	9.6

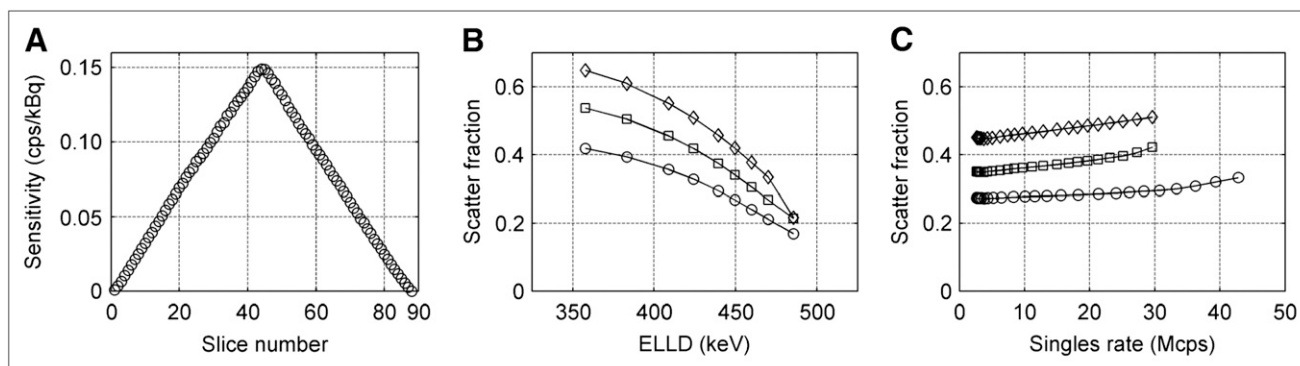


FIGURE 3. (A) Triangular sensitivity profile as measured with NEMA NU2-2001 line source. (B) Plot of measured *SF* as function of ELLD for 3 different cylinder diameters. Plots with symbols \circ , \square , and \diamond are for cylinder diameters of 20, 27, and 35 cm, respectively. (C) Plot of *SF* as function of singles rate in scanner. Plots with symbols \circ , \square , and \diamond are for cylinder diameters of 20, 27, and 35 cm, respectively. Currently, clinical imaging is performed at a singles rate of 15–25 Mcps.

image for TOF reconstruction with similar *CRC* as in non-TOF reconstruction. With the larger 35-cm-diameter phantom it is very clear that the *CRC/Noise* curves with TOF reconstruction lie above the non-TOF reconstructions for the scan time shown here. These results indicate that TOF reconstruction has greater benefit in big objects with fast convergence to high *CRC* values.

Patient Studies. Figure 7A shows a plot of patient weight against the measured diameter in the reconstructed images. There is a strong linear correlation as indicated by the linear fit shown in the plot. In particular, the 20-, 27-, and

35-cm-diameter patients correspond to patient weights of 40, 60, and 95 kg, respectively. The *SF* for these patients as estimated through the SSS algorithm varies between 30% and 50% and lies within the range of *SF* values measured for the 3 cylindric phantoms (diameters of 20, 27, and 35 cm). Figure 7B is a plot of calculated patient *NEC'* versus the patient diameter. The patients were scanned 60 min after injection of 555 MBq (15 mCi) of ^{18}F -FDG. For 20-, 27-, and 35-cm-diameter patient sizes this corresponds to activity concentrations of 9.4 kBq/mL (0.26 $\mu\text{Ci/mL}$), 6.3 kBq/mL (0.17 $\mu\text{Ci/mL}$), and 4.0 kBq/mL (0.11 $\mu\text{Ci/mL}$),

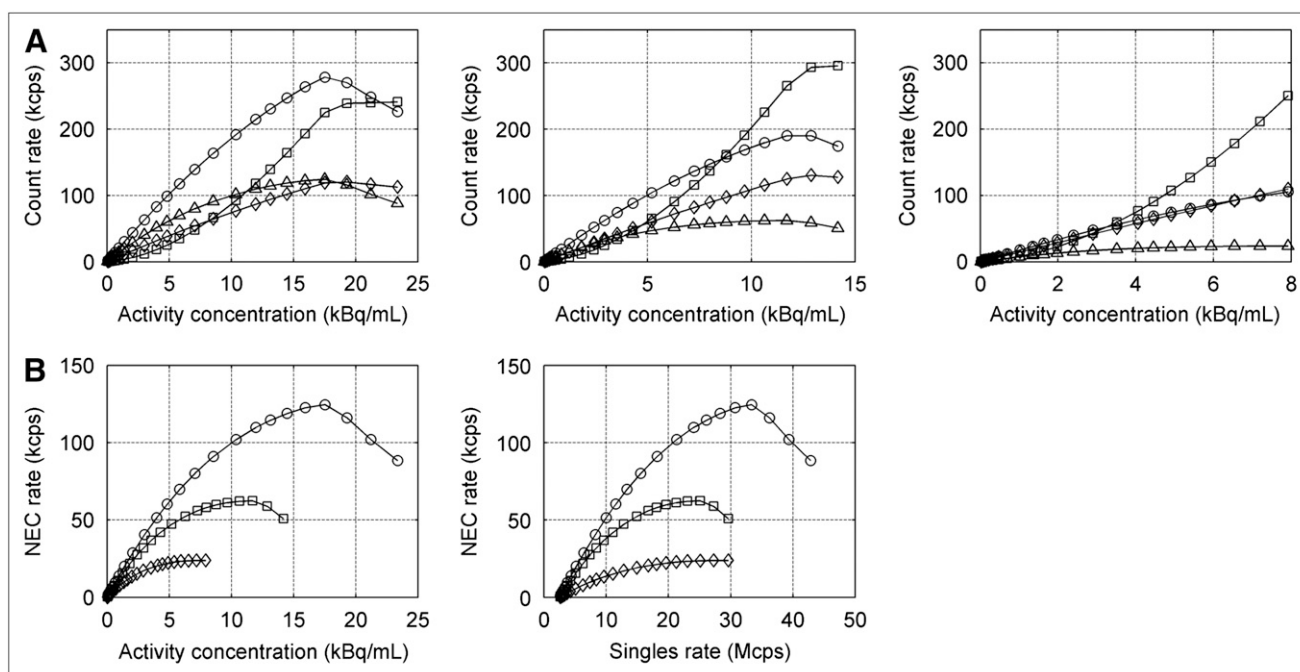


FIGURE 4. (A) Plot of counting rates as function of activity concentration for (moving left to right) 20-, 27-, and 35-cm-diameter cylinders. Plots with symbols \circ , \square , \diamond , and \triangle are for true coincidence rate, random coincidence rate, scatter coincidence rate, and *NEC* rate, respectively. (B) Summary plots for *NEC* rate shown both as function of activity concentration and singles rate in scanner (left and right, respectively). Plots with symbols \circ , \square , and \diamond are for 20-, 27-, and 35-cm-diameter cylinders, respectively. Currently, clinical imaging is performed at a singles rate of 15–25 Mcps.

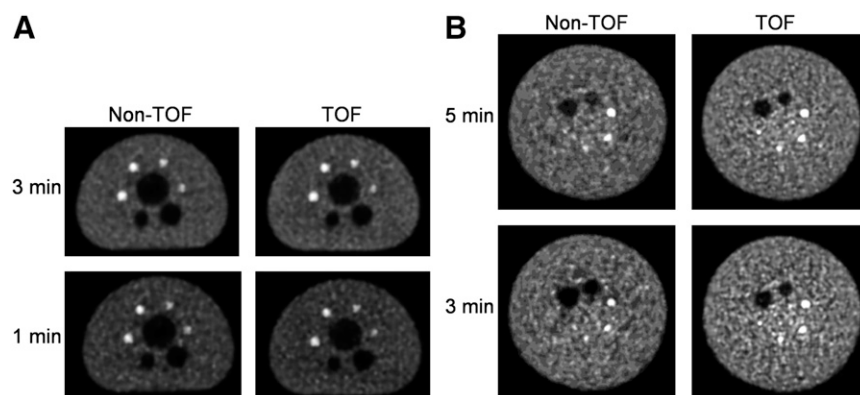


FIGURE 5. (A) Representative slices from reconstructed images of NEMA torso phantom using TOF and non-TOF IRX algorithms for 2 different scan times. (B) Representative slices from reconstructed images of larger 35-cm-diameter phantom using TOF and non-TOF UPenn algorithms for 2 different scan times. All images shown here are after 10 iterations of reconstruction (subsets = 20, $\lambda = 1$).

respectively. The line in Figure 7B shows the NEC' numbers for the 3 cylindric phantoms at these activity concentrations. As can be seen, there is a good correlation between the patient and phantom data. This correlation gives us confidence that we can use phantom data to modify patient dose protocols and predict corresponding counting rates.

Figure 7C shows 2 coronal slices of the reconstructed images for the light patient (61 kg, BMI of 22.2) using data from the first 1 and 3 min of the acquisition. This patient had head and neck cancer with lesions present in the liver and spine regions as well. Though the 1-min scan time per bed position images are noisier, they still retain good noise characteristics in the reconstructed images. Figure 7D shows 2 coronal slices of the reconstructed images for the heavy patient (115 kg, BMI of 38.0) also using data from the first 1 and 3 min of the acquisition. This patient was diagnosed with abdominal cancer. Now the 3 min per bed position images appear noticeably better in noise characteristics compared with the 1 min per bed position images. Note that all of these patient images are reconstructed with the commercial TOF reconstruction algorithm (DLT) provided by the manufacturer. Relating these patient data to the plots shown in Figures 7A and 7B, we see that the light patient data correspond to an NEC' rate of about 120 kcps, whereas the heavy patient data correspond to an NEC' rate of about 60 kcps. Note, the SF is not included in the

calculation of NEC' and is higher for the heavy patient. The image after 1-min scan time for the light patient looks satisfactory in terms of image quality, whereas for the heavy patient image a 3-min scan is more appropriate.

DISCUSSION

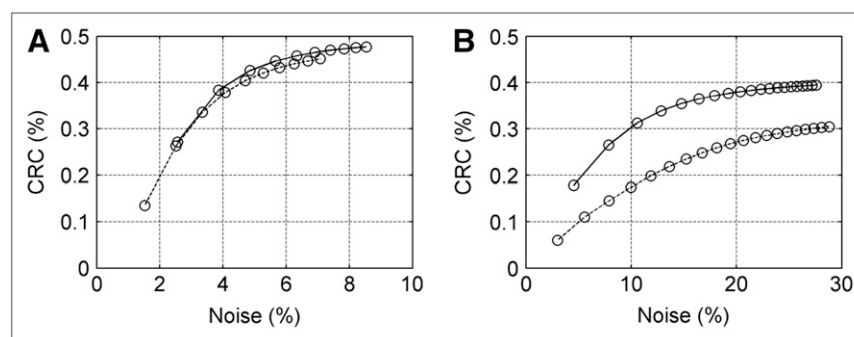
The Philips Gemini TF PET/CT incorporates a new, high-performance TOF-capable PET scanner with very good conventional non-TOF PET capabilities as well. As shown in previous work (23), the use of an Anger-logic detector with a uniform light spread in the detector leads to very good system energy and timing resolutions. As a result, the lower threshold of the energy window is set high at 440 keV, leading to reduced scattered events in the collected data. The use of a fast, dense, and high light output scintillator (LYSO) leads to high sensitivity, reduced scanner dead time, and good spatial resolution. Basic performance measurements according to NEMA NU2-2001 procedure show that the system spatial resolution is 4.8 mm near the scanner center and the absolute system sensitivity is 6.6 cps/kBq.

SF measurements using the NEMA NU2-2001 cylinder (20-cm diameter by 70-cm line source cylinders) show a value of 27%. Because this cylinder represents an equivalent of a light patient, we repeated these measurements on larger phantoms with diameters of 27 cm and 35 cm

TABLE 2
CRC and Variability Numbers from NEMA/IEC Torso Phantom Reconstructions for 3-Minute Scan Time

Reconstruction algorithm	Iteration no.	Parameter	Sphere diameter (mm)					
			10	13	17	22	28	37
UPenn TOF	6	CRC (%)	35	47	70	69	74	82
		Variability (%)	6.9	6.1	5.2	4.4	3.9	3.2
UPenn non-TOF	6	CRC (%)	31	42	69	70	71	82
		Variability (%)	5.7	5.2	4.6	3.9	3.1	2.5
DLT	3	CRC (%)	35	44	66	65	59	70
		Variability (%)	4.8	4.6	4.1	3.7	3.3	3.0
LOR RAMLA	2	CRC (%)	23	34	60	62	68	78
		Variability (%)	6.3	5.9	5.1	4.4	3.6	2.9

FIGURE 6. Plots for CRC vs. Noise values calculated for (A) NEMA torso phantom and (B) 35-cm-diameter image-quality phantom. Results are shown for 13-mm-diameter hot sphere and 3-min scan time. Plots with solid lines are TOF, whereas dotted lines are non-TOF reconstruction. Points along each curve represent increasing number of iterations of reconstruction algorithm with lower left point being iteration 1 and upper right point being iteration 10 in A and iteration 20 in B.



(representative of average and heavy patients). Increased scatter in these situations is indicated with measured *SF* values of 35% and 45%, respectively. Our *NEC* plots (Fig. 4B) show that the peak *NEC* rate with the NEMA phantom is 125 kcps and occurs at an activity concentration of 17.4 kBq/mL (0.47 μ Ci/mL). However, increased attenuation as well as random and scatter coincidences lead to a noticeable drop in the peak *NEC* values for the 2 larger phantoms. Currently, clinical images are acquired at a singles rate of

15–25 Mcps, which is below the singles range (30–35 Mcps) at which the *NEC* peaks for all 3 phantoms.

The timing resolution of this scanner after recent calibration upgrades is 585 ps. Daily quality control measurements spread out over several months show that the electronics are stable without any significant variations. This is an important characteristic as the TOF PET scanners developed in the 1980s had significant calibration issues that led to a degradation in the system timing resolution over time (24).

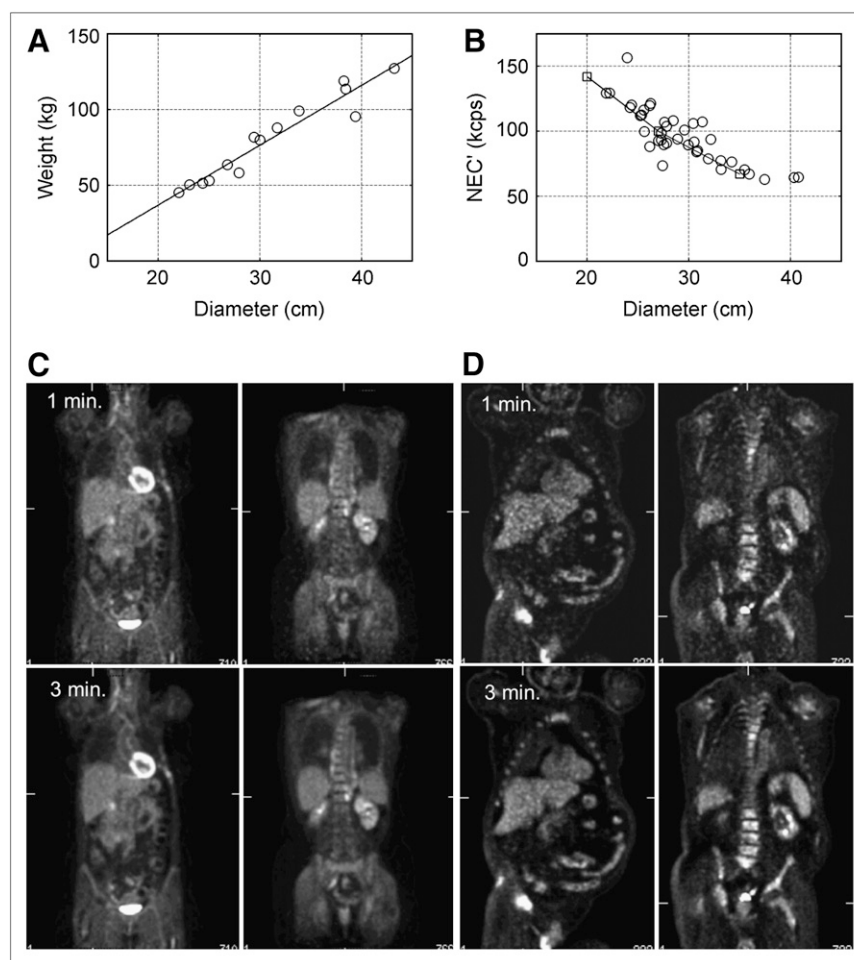


FIGURE 7. (A) Plot of patient weight vs. diameter as measured in reconstructed image. There is strong correlation between these two as shown by dotted line that is a linear fit to data. (B) Plot of *NEC'* vs. diameter for patient data (\circ). In addition, we also plotted data for 20-, 27-, and 35-cm-diameter cylindric phantoms as square symbols connected by a solid line for activity concentrations corresponding to similar patient size. (C) Coronal image for light patient (61 kg) with head and neck cancer and lesions in liver and spine. Patient was injected with 518 MBq (14.0 mCi) of ^{18}F -FDG 60 min before scan time. Images are shown for 1 min per bed position (top row) and 3 min per bed position (bottom row). (D) Coronal image for heavy patient (115 kg) with abdominal cancer. Patient was injected with 537 MBq (14.5 mCi) of ^{18}F -FDG 60 min before scan time. Images are shown for 1 min per bed position (top row) and 3 min per bed position (bottom row).

Because the NEMA NU2-2001 measurements are performed for low counting rate situations (other than the NEC measurements) and non-TOF PET scanners, measurements characterizing timing resolution performance in TOF PET scanners are not prescribed. We have proposed a technique using a centrally positioned ^{22}Na point source placed next to cylinders filled with water and high ^{18}F activity to estimate the energy, spatial, and timing resolution in the scanner as a function of counting rate. This technique allows us to quantify the scanner timing resolution at low activity levels (almost no ^{18}F activity in the cylinders) as well as characterize the impact of pulse pileup on energy, spatial, and timing resolution as a function of the singles rate. Because these are not accounted for in the NEC calculation, this measurement represents an added characterization of the scanner performance at high counting rate (TOF as well as non-TOF) that will affect the resultant image quality. Our results show that at clinical imaging rates (singles rate of 15–25 Mcps) the timing resolution of this scanner is in the range of 650–700 ps. For imaging with short-lived isotopes (e.g., ^{11}C , ^{13}N , ^{82}Rb) with higher injected dose than typical ^{18}F -FDG studies, the timing resolution would potentially degrade further—note that at the peak NEC rate (singles rate of 25–35 Mcps) the timing resolution is 750–800 ps.

Our image-quality measurements show that TOF benefit is not well realized in the NEMA torso phantom. This is presumably due to the relatively small size of this phantom with respect to the timing resolution of this scanner. It has been shown in previous studies (25–27) that the gain in image quality with TOF information is proportional to the object size and inversely proportional to the system timing resolution. The results with the 35-cm-diameter phantom clearly indicate the benefit of TOF PET in imaging heavy or large objects. The TOF images converge faster (smaller number of iterations or noise in the image) to high CRC values for large objects. In addition, the detectability of small lesions is increased with the TOF information. The improved image quality with TOF information is an active ongoing research area, and a thorough investigation is beyond the scope of this article. With the change in timing resolution due to pulse pileup at high counting rates, it adds an additional aspect to the efforts involving the characterization of TOF PET image quality.

The CRC results from the commercial DLT algorithm are, as expected, similar to the TOF UPenn results for the hot spheres. However, the reduced CRC values for the cold 28- and 37-mm-diameter spheres with DLT compared with the TOF UPenn algorithm are due to the use of a non-TOF version of scatter correction that is currently used on this scanner.

Clinical imaging protocols at our institution are not completely optimized, but the initial correlation between phantom and patient counting rate data will allow us to do so in the near future. Currently, clinical imaging with ^{18}F -FDG is performed with a dose of 555 MBq (15 mCi) and a postinjection scan time of 1 h, which results in a singles

rate range of 15–22 Mcps. This is below the singles rate at which the NEC rate peaks for the 3 cylindric phantoms we investigated in this work (25–35 Mcps). Our results show that for small and average patient sizes, 1–2 min per bed position will translate into a 10- to 20-min scan time per patient and lead to satisfactory image quality. For heavier patients with increased attenuation, we prefer to image for 3 min per bed position or 30-min total scan time.

CONCLUSION

In this work we characterized the performance of the PET component of a new PET/CT scanner. The PET scanner represents the first commercial version of a fully 3D TOF PET scanner used for clinical whole-body imaging. Besides having very good conventional imaging capabilities, this scanner also has a timing resolution of about 600 ps, which allows its use as a routine TOF PET scanner. Our results show that there is an improvement in image quality with TOF information, which greater benefits heavy patients. Additional work is ongoing to fully understand the TOF benefit for resultant images and its impact on clinical diagnosis.

ACKNOWLEDGMENTS

We thank members of the Physics and Instrumentation Group at the University of Pennsylvania and the PET engineering team from the Nuclear Medicine Division of Philips Medical Systems for their technical and scientific help with this work. This research was supported by National Institutes of Health grant R33-EB001684 and a sponsored research agreement with Philips Medical Systems.

REFERENCES

1. NEMA Standards Publication NU2-2001: Performance Measurements of Positron Emission Tomographs. Rosslyn, VA: National Electrical Manufacturers Association; 2001.
2. Surti S, Karp JS, Freifelder R, Liu F. Optimizing the performance of a PET detector using discrete GSO crystals on a continuous lightguide. *IEEE Trans Nucl Sci.* 2000;47:1030–1036.
3. Karp JS, Surti S, Daube-Witherspoon ME, et al. Performance of a brain PET camera based on Anger-logic gadolinium oxyorthosilicate detectors. *J Nucl Med.* 2003;44:1340–1349.
4. Surti S, Karp JS. Imaging characteristics of a 3-dimensional GSO whole-body PET camera. *J Nucl Med.* 2004;45:1040–1049.
5. Gregory R, Partridge M, Flower MA. Performance evaluation of the Philips “Gemini” PET/CT system. *IEEE Trans Nucl Sci.* 2006;53:93–101.
6. Turcotte E, Lepage M, Croteau E, Kolthammer J, Gagnon D, Benard F. Performance evaluation of a new Zr-GSO PET/CT scanner based on the NEMA NU 2-2001 standard [abstract]. *J Nucl Med.* 2005;46(suppl 2):206P–207P.
7. Griesmer J, Laurence T, Cooke S, Karp J, Perkins A, Kolthammer J. Time-of-flight quality control for a new Philips Gemini PET/CT scanner [abstract]. *J Nucl Med.* 2006;47(suppl 1):391P–392P.
8. Badawi RD, Domigan P, Johnson O, et al. Count-rate dependent event mispositioning and NEC in PET. *IEEE Trans Nucl Sci.* 2004;51:41–45.
9. Vaska P, Alexoff DL. Effects of natural LSO radioactivity on microPET quantitation [abstract]. *J Nucl Med.* 2003;44(suppl):138P.
10. Watson CC, Casey ME, Eriksson L, Mulnix T, Adams D, Bendriem B. NEMA NU 2 performance tests for scanners with intrinsic radioactivity. *J Nucl Med.* 2004;45:822–826.

11. Matej S, Lewitt RM. Direct Fourier reconstruction with Fourier reprojction for fully 3-D PET. *IEEE Trans Nucl Sci.* 2001;48:1378–1385.
12. Bailey DL, Jones T, Spinks TS. A method for measuring the absolute sensitivity of positron emission tomographic scanners. *Eur J Nucl Med.* 1991;18:374–379.
13. Daube-Witherspoon ME, Muehllehner G. Treatment of axial data in three-dimensional PET. *J Nucl Med.* 1987;28:1717–1724.
14. Surti S, Badawi RD, Holdsworth CH, El Fakhri G, Kinahan PE, Karp JS. A multi-scanner evaluation of PET image quality using phantom studies. Paper presented at: 2003 IEEE Nuclear Science Symposium and Medical Imaging Conference; October 19–25, 2003; Portland, OR.
15. Conti M. Effect of randoms on signal-to-noise ratio in TOF PET. *IEEE Trans Nucl Sci.* 2006;53:1188–1193.
16. Popescu LM. Iterative image reconstruction using geometrically ordered subsets with list-mode data. Paper presented at: 2004 IEEE Nuclear Science Symposium and Medical Imaging Conference; October 16–22, 2004; Rome, Italy.
17. Popescu LM, Lewitt RM. Tracing through a grid of blobs. Paper presented at: 2004 IEEE Nuclear Science Symposium and Medical Imaging Conference; October 16–22, 2004; Rome, Italy.
18. Accorsi R, Adam LE, Werner ME, Karp JS. Optimization of a fully 3D single scatter simulation algorithm for 3D PET. *Phys Med Biol.* 2004;49:2577–2598.
19. DePierro AR. On some nonlinear iterative relaxation methods in remote sensing. *Matematica Aplicada e Computacional.* 1989;8:153–166.
20. Browne JA, DePierro AR. A row-action alternative to the EM algorithm for maximizing likelihoods in emission tomography. *IEEE Trans Med Imaging.* 1996;15:687–699.
21. Matej S, Browne JA. Performance of a fast maximum likelihood algorithm for fully-3D PET reconstruction. In: Grangeat P, Amans J-L, eds. *Three Dimensional Image Reconstruction in Radiology and Nuclear Medicine.* Dordrecht, Netherlands: Kluwer Academic Publishers; 1996:297–316.
22. Watson CC. Extension of single scatter simulation to scatter correction of time-of-flight PET. Paper presented at: 2005 IEEE Nuclear Science Symposium and Medical Imaging Conference; October 23–29, 2005; San Juan, Puerto Rico.
23. Kuhn A, Surti S, Karp JS, et al. Design of a lanthanum bromide detector for time-of-flight PET. *IEEE Trans Nucl Sci.* 2004;51:2550–2557.
24. Lewellen TK. Time-of-flight PET. *Semin Nucl Med.* 1998;28:268–275.
25. Surti S, Karp JS, Popescu LA, Daube-Witherspoon ME, Werner M. Investigation of time-of-flight benefit for fully 3-D PET. *IEEE Trans Med Imaging.* 2006;25:529–538.
26. Budinger TF. Time-of-flight positron emission tomography: status relative to conventional PET. *J Nucl Med.* 1983;24:73–76.
27. Tomitani T. Image-reconstruction and noise evaluation in photon time-of-flight assisted positron emission tomography. *IEEE Trans Nucl Sci.* 1981;28:4582–4589.



The Journal of
NUCLEAR MEDICINE

Performance of Philips Gemini TF PET/CT Scanner with Special Consideration for Its Time-of-Flight Imaging Capabilities

Suleman Surti, Austin Kuhn, Matthew E. Werner, Amy E. Perkins, Jeffrey Kolthammer and Joel S. Karp

J Nucl Med. 2007;48:471-480.


This article and updated information are available at:
<http://jnm.snmjournals.org/content/48/3/471>

Information about reproducing figures, tables, or other portions of this article can be found online at:
<http://jnm.snmjournals.org/site/misc/permission.xhtml>

Information about subscriptions to JNM can be found at:
<http://jnm.snmjournals.org/site/subscriptions/online.xhtml>

The Journal of Nuclear Medicine is published monthly.
SNMMI | Society of Nuclear Medicine and Molecular Imaging
1850 Samuel Morse Drive, Reston, VA 20190.
(Print ISSN: 0161-5505, Online ISSN: 2159-662X)

© Copyright 2007 SNMMI; all rights reserved.

 SOCIETY OF
NUCLEAR MEDICINE
AND MOLECULAR IMAGING